

Article

Mononuclear Heptacoordinated 3d-Metal Helicates as a New Family of Single Ion Magnets

Yulia P. Tupolova ¹, Denis V. Korchagin ², Anastasya S. Andreeva ¹, Valery V. Tkachev ², Gennadii V. Shilov ², Vladimir A. Lazarenko ³, Leonid D. Popov ¹, Konstantin A. Babeshkin ⁴, Nikolay N. Efimov ⁴, Roman B. Morgunov ², Andrei V. Palii ², Stanislav P. Kubrin ¹, Igor N. Shcherbakov ¹, and Sergey M. Aldoshin ^{2,*}

¹ Department of Chemistry, Southern Federal University, 7, Zorge Str., 344090 Rostov-on-Don, Russia

² Federal Research Center of Problems of Chemical Physics and Medicine Chemistry, Russian Academy of Sciences, 1, Acad. Semenov Av., 142432 Chernogolovka, Russia

³ National Research Center “Kurchatov Institute”, 1, Acad. Kurchatov Sq., 123182 Moscow, Russia

⁴ N. S. Kurnakov Institute of General and Inorganic Chemistry, Russian Academy of Sciences, 31, Leninsky Prosp., 119991 Moscow, Russia

* Correspondence: sma@icp.ac.ru

Abstract: The series of Co(II), Fe(II), and Ni(II) mononuclear coordination compounds of [CoL(NCS)₂]-3DMSO (**1**), [CoL(H₂O)₂](ClO₄)₂·DMSO (**2**), [CoL(H₂O)(EtOH)][CoCl₄]-2H₂O (**2a**), [FeL(NCS)₂]-DMSO (**3**), and [NiL(NCS)₂]-CH₃CN (**4**) composition (where L is 2,6-bis(1-(2-(4,6-dimethylpyrimidin-2-yl)hydrazineylidene)ethyl)pyridine), with an [MLA₂] coordination unit (where A is a pair of apical monodentate ligands), was synthesized. In compounds **1**, **2**, **2a**, and **3**, the ligand L is pentadentate, and cobalt and iron ions are placed in a heavily distorted pentagonal pyramidal coordination environment, while in **4** the Ni(II) ion is hexacoordinated. Easy plane-type magnetic anisotropy ($D = 13.69, 11.46, 19.5,$ and 6.2 cm^{-1} for **1**, **2**, **2a**, and **4**, respectively) was established for cobalt and nickel compounds, while easy axis-type magnetic anisotropy ($D = -14.5 \text{ cm}^{-1}$) was established for iron compound **3**. The cobalt coordination compounds **1** and **2** show SIM behavior under a 1500 Oe external magnetic field, with effective magnetization reversal barriers of 65(1) and 60(1) K for **1** and **2**, respectively. The combination of Orbach and Raman relaxation mechanisms was shown to adequately describe the temperature dependence of relaxation times for **1** and **2**. CASSCF/NEVPT2 calculations were performed to model the parameters of the effective spin Hamiltonian for the compounds under study.

Keywords: single-ion magnets; magnetic anisotropy; ab initio calculation; crystal field theory; spin-orbit coupling; single-crystal X-ray diffraction study



Citation: Tupolova, Y.P.; Korchagin, D.V.; Andreeva, A.S.; Tkachev, V.V.; Shilov, G.V.; Lazarenko, V.A.; Popov, L.D.; Babeshkin, K.A.; Efimov, N.N.; Morgunov, R.B.; et al. Mononuclear Heptacoordinated 3d-Metal Helicates as a New Family of Single Ion Magnets. *Magnetochemistry* **2022**, *8*, 153. <https://doi.org/10.3390/magnetochemistry8110153>

Academic Editor: Fabrice Pointillart

Received: 3 October 2022

Accepted: 2 November 2022

Published: 9 November 2022

Publisher's Note: MDPI stays neutral with regard to jurisdictional claims in published maps and institutional affiliations.



Copyright: © 2022 by the authors. Licensee MDPI, Basel, Switzerland. This article is an open access article distributed under the terms and conditions of the Creative Commons Attribution (CC BY) license (<https://creativecommons.org/licenses/by/4.0/>).

1. Introduction

Heptacoordinated “late” 3d-row metal ions in a pentagonal bipyramidal (PBY) coordination environment were found to be good candidates for exhibiting single-ion magnet (SIM) properties [1–3]. SIM compounds are a subset of the broader family of single-molecule magnets (SMMs), in which the magnetization storage is limited to single paramagnetic centers (d- or f-metal ions) [4–6]. SIMs have been continuously attracting the interest of the coordination chemistry community for the past three decades [7–11] due to the promising revolutionary introduction of these materials into cutting-edge technologies of ultrahigh-density memory storage [12,13], molecular spintronics [14,15], quantum computing, and information processing [16–18], as well as other applications and devices [19–22]. The 3d-metals are attractive as SIM cores because of their rich coordination chemistry and their ability to modify the electronic and spin distribution and to control the shape of coordination polyhedrons via the appropriate design of polydentate organic ligands [23,24], as well as because of the availability of powerful quantum chemical approaches suitable for the quantitative prediction and analysis of magnetic anisotropy [1,24–28]. The latter

approaches are of valuable help in achieving in-depth understanding of the correlations between structural features of the compounds and their magnetic properties.

PBY-type heptacoordination is not common for the “late” 3d-row transition metal ions due to their rather small ionic radii; however, in Cambridge Structural Database (CSD [29]), there are at least 450 structures solved by single-crystal X-ray diffraction analysis, the majority of which are based on the condensation products of 2,6-diacetyl (2,6-diformyl) pyridine with various carboxylic acid hydrazides and similar ONNNO-type acyclic pentadentate organic molecules [30,31] (see the recent review of Sutter et al. [32]). Due to terminal O-donor atoms, the compounds with these ligands are close to the planar conformation. The easy plane-type magnetic anisotropy (positive axial zero-field splitting (ZFS) parameter D) is usual for Co compounds, while for Fe and Ni compounds the easy axis-type anisotropy ($D < 0$) typically occurs. The 15-membered macrocyclic organic molecules with NNNNO function, which are topologically analogous to the 15-crown-5 ligand family, are also popular as ligands.

N-pentadentate ligands appropriate for the construction of heptacoordinated compounds have been studied on a much smaller scale. The majority of the available coordination compounds are based on 15-membered macrocyclic organic molecules. Several compounds were synthesized with quinquepyridine-derived ligands [33,34], and their interaction with magnetic fields was not studied. Recently [35,36], a heptadentate ligand was used to obtain a field-induced Co(II) SIM, which favors a distorted capped trigonal prism environment. Steric crowding of the terminal nitrogen donors in the case of the acyclic NNNNN-pentadentate ligand leads to the formation of a helical-like structure of the coordinated ligand.

In this paper, we report the synthesis of heptacoordinated Co, Fe, and Ni mononuclear helicates with an $[MLA_2]$ coordination unit, where **L** is 2,6-bis(1-(2-(4,6-dimethylpyrimidin-2-yl)hydrazineylidene)ethyl)pyridine (NNNNN-pentadentate ligand) and **A** is a pair of apical monodentate ligands.

2. Results and Discussion

2.1. Synthesis

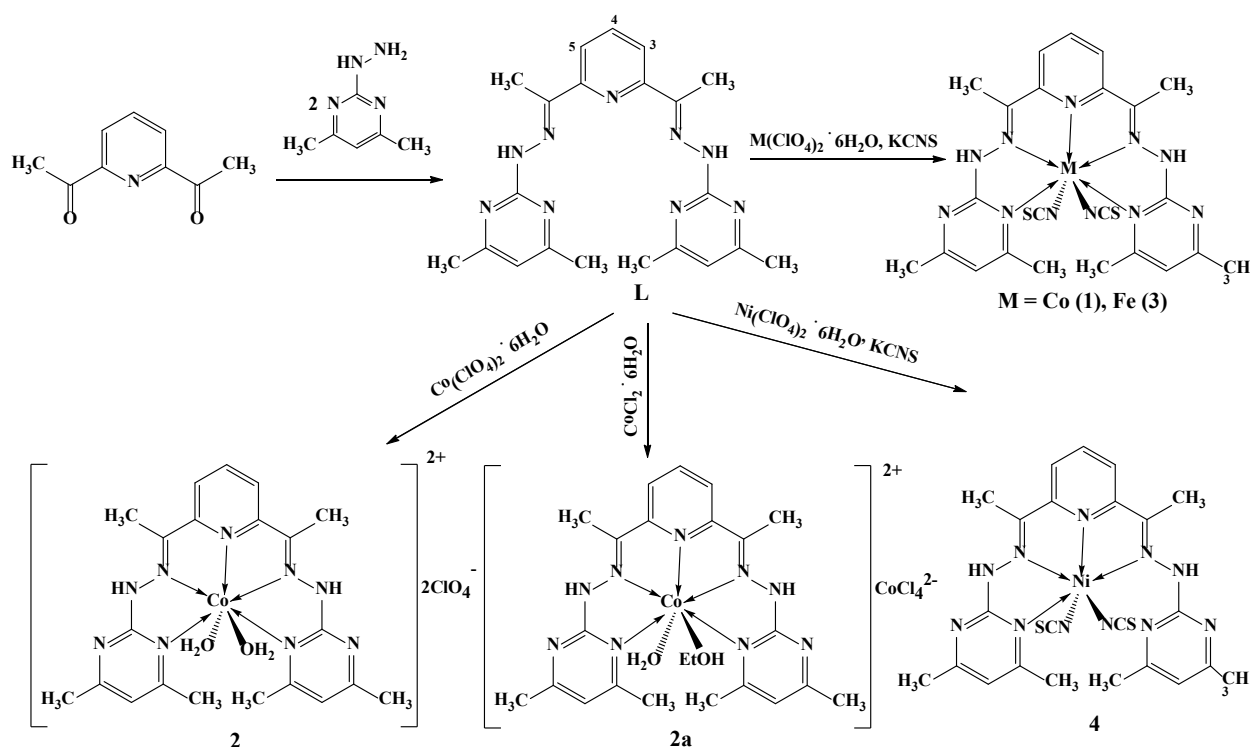
Bis-hydrazone of 2,6-diacetylpyridine and 4,6-dimethyl-2-hydrazinopyrimidine (**L**), along with coordination compounds, were obtained as shown in Scheme 1.

Reaction of **L** with Co(II), Fe(II), and Ni(II) perchlorates in methanol solution in the presence of potassium thiocyanate yielded coordination compounds containing a neutral coordination unit $[ML(NCS)_2]$ ($M = \text{Co}$ (**1**), Fe (**3**), Ni (**4**)), consisting of the polydentate ligand **L** and two isothiocyanate ligands. The following single-crystal samples were obtained after crystallization as solvates: $[\text{CoL}(\text{NCS})_2] \cdot 3\text{DMSO}$ (**1**), $[\text{FeL}(\text{NCS})_2] \cdot \text{DMSO}$ (**3**), and $[\text{NiL}(\text{NCS})_2] \cdot \text{CH}_3\text{CN}$ (**4**), respectively.

In the absence of potassium thiocyanate upon the reaction of **L** with Co(II) perchlorate in methanol solution, diaquadicationic coordination species were formed, which upon crystallization from DMSO solution were obtained as a DMSO solvate of the perchlorate salt $[\text{CoL}(\text{H}_2\text{O})_2](\text{ClO}_4)_2 \cdot \text{DMSO}$ (**2**). One of the coordinated water molecules in the crystals of **2** is statistically replaced by a methanol molecule (water: methanol molar ratio of 75:25).

A similar aqua–ethanol complex containing the dication $[\text{CoL}(\text{H}_2\text{O})(\text{EtOH})]^{2+}$ was formed upon the reaction of **L** with Co(II) chloride. In this case, the role of a counteranion was played by the tetrachlorocobaltate dianion $[\text{CoCl}_4]^{2-}$. The composition of the obtained product was $[\text{CoL}(\text{H}_2\text{O})(\text{EtOH})][\text{CoCl}_4] \cdot 2\text{H}_2\text{O}$ (**2a**).

The structure of the reaction product of **L** with Co(II) bromide was not solved completely, due to a strong disorder of the solvate molecules and bromide anions in the crystals, but the structure of the coordinated unit was determined unambiguously as $[\text{CoL}(\text{H}_2\text{O})_2]^{2+}$; bromide anions were outside of the metal coordination sphere and were not coordinated to the Co(II) cations (the best obtained molecular structure of the product is shown in Figure S1 of the Supplementary Materials and is not discussed in the paper).



Scheme 1. Synthesis of the compounds.

Thus, chloride, bromide, and perchlorate anions do not enter the coordination sphere of the Co(II) ion, and upon the reaction with the corresponding salts, dicationic complex species are formed with coordinated solvent molecules (i.e., water, methanol, and ethanol). Considering the larger ionic radii of Cl^- and Br^- compared to O (in the solvent molecules) and N (in NCS^-), one of the possible explanations of such behavior could be the decreased accessibility of the apical positions for the coordination of relatively large monoanions due to heavy, helix-like distortion of the plane of ligand L, while coordination of NCS^- and the solvent molecule ligands remains possible.

In case of cobalt (1,2,2a) and iron (3) complexes, L acts as a pentadentate ligand, while in the case of the nickel (4) compound, only four coordination bonds are formed by L with the metal center, limiting the coordination number of Ni(II) in this complex to six. The tendency of Ni(II) to avoid the PBV-type heptacoordination is rationalized in [37].

2.2. Crystal Structure

For five complexes, single-crystal X-ray diffraction experiments were performed. In compounds 1–3, heptacoordinated Co(II) and Fe(II) ions formed a distorted coordination polyhedron that was closest to pentagonal bipyramidal (continuous symmetry measure PBPY-7, in the case of compounds 1 and 3) and capped trigonal prism symmetry (continuous symmetry measure CTPR-7, in the case of compounds 2 and 2a), according to the results of the SHAPE 2.1 program analysis [38,39], which are presented in Table S1 of the Supplementary Materials. The pentadentate ligand was coordinated through one nitrogen atom of pyridine, two nitrogen atoms of pyrimidine, and two nitrogen atoms of hydrazone fragments and arranged around the metal center in the form of half-helix due to the steric repulsion of the methyl groups of the terminal pyrimidine moieties of bis-hydrazone L. In compounds 1 and 3, the apical positions were populated by NCS^- anions and the coordination units were neutral. In compounds 2 and 2a, one apical position was filled by a coordinated water molecule, while the other was populated by water molecules (75%) and by methanol molecules (25%) in the case of compound 2, and by ethanol molecules in the case of 2a. In contrast to 1 and 3, the coordination units in 2 and 2a were cationic, while the counterions were two ClO_4^- anions in the case of 2 and $[\text{CoCl}_4]^{2-}$ in the case of

2a. In compound **4**, the Ni(II) ion was hexacoordinated, and the shape of the coordination polyhedron was closest to distorted octahedral symmetry (Table S1, Supplementary Materials). The nitrogen atom of one of the pyrimidine cycles was not coordinated and, due to rotation of the pyrimidine fragment around the N-N bond of the hydrazone moiety, was significantly far from the metal center. The apical positions in the compound were filled with NCS^- anions. The coordination unit in **4**, similar to **1** and **3**, was uncharged.

The molecular structure of compounds **1–3** is shown in Figure 1 (as an illustration of the structure and numbering scheme used in this discussion, the molecular structure of compound **1** is shown; the exact molecular structures of compounds **2**, **2a**, and **3** are shown in Table S2 of the Supplementary Materials). The pentadentate ligand is nonplanar. Distortion of the planar structure is caused by steric repulsion of the methyl groups of the pyrimidine rings, resulting in rotation around the N-N and N-C bonds of the hydrazinopyrimidine moiety to the opposite sides of the ligand's plane; the corresponding torsion angles C(6)N(2)N(3)C(8), C(14)N(6)N(7)C(16) and N(2)N(3)C(8)N(4), N(6)N(7)C(16)N(8) in compound **1** are 169.3, 167.8 and 6.8, 1.1°, respectively. In compound **2** these angles are 164.2, 161.6 and 6.5, 11.2°, in compound **2a** they are 169.0(2), 165.9(2) and 4.3(3), 7.3(3), and in compound **3** they are 175.5 and 7.5°, respectively. Due to the abovementioned distortions, the intramolecular distance between the carbon atoms of the methyl groups C(13) ... C(21) is increased to 3.538 Å. The corresponding distances in **2**, **2a**, and **3** are 3.937, 3.783, and 3.261 Å, respectively. The dihedral angles between the pyrimidine cycles in **1**, **2a**, and **3** are 41.0, 51.6, 46.1, and 35.5°, respectively.

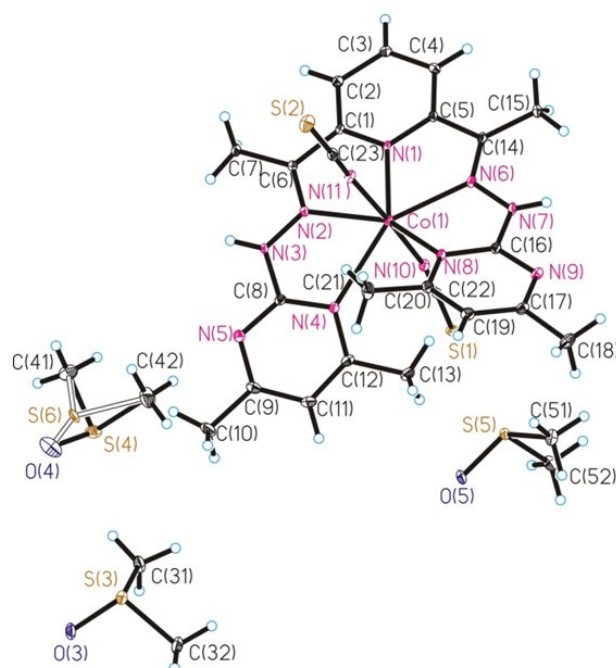


Figure 1. Molecular structure and atom-numbering scheme of compound **1** (for convenience, the same atom numbering is used when discussing complexes **2**, **2a**, and **3**).

The pentadentate ligand in **1–3** forms four five-membered metallacycles. The coordination bond lengths (M–N) are in the range of 2.139(3)–2.492(3) Å (see Table 1); the shortest is the Co–N bond with the nitrogen atom of the pyridine cycle (2.139(3) Å in **2**), while the most elongated is with the nitrogen atoms of the pyrimidine substituents (2.492(3) in **1** and 2.481(3) Å in **3**).

Table 1. Interatomic M–N distances (Å) in compounds 1–3 (M = Co (1,2); Fe (3)).

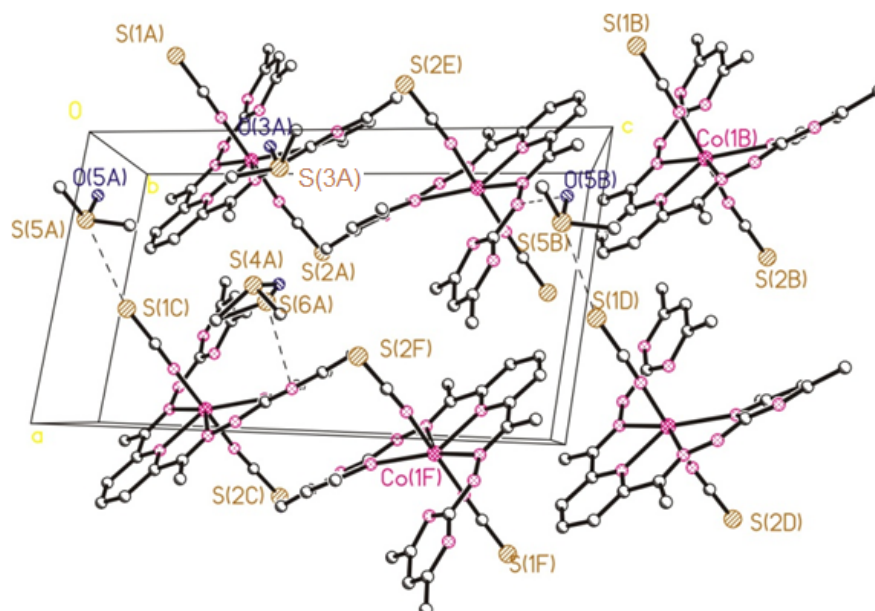
Comp.	M–N(1)	M–N(2)	M–N(4)	M–N(6)	M–N(8)	M–N(10)	M–N(11)
1	2.178(3)	2.271(3)	2.492(3)	2.215(3)	2.336(3)	2.095(3)	2.085(3)
2	2.139(3)	2.143(3)	2.223(3)	2.157(3)	2.238(3)	-	-
2a	2.155(2)	2.172(2)	2.230(2)	2.171(2)	2.325(2)	2.157(2) O(H ₂ O) ¹	2.184(2) O(EtOH) ¹
3	2.240(3)	2.318(2)	2.481(2)	2.318(2)	2.481(2)	2.095(2)	2.095(2)

¹ For compound 2a, the distances to apical water and ethanol ligands are shown.

In 1 and 3, the apical positions are populated by two NCS[−] groups (interatomic M–N distances are shown in Table 1). Angle N(10)–M–N(11) = 177.38(12) (in 1) and 173.66(13)[°] (in 3), while angle S(2)–C(23)–N(11) = 178.5(3) and S(1)–C(22)–N(10) = 177.9(3)[°] in 1, and both angles in 3 are 178.9(3)[°].

In compound 2, the apical positions contain oxygen atoms; in one of them it is the oxygen atom of the water molecule (atom O(1)), and in the other position it is 75% of the oxygen atom of the coordinated water molecule and 25% of the coordinated methanol molecule (O(2) atom). The bond lengths Co–O(1) = 2.223(3) and Co–O(2) = 2.212(3) Å. The bond angle O(1)–Co(1)–O(2) is 166.30(12)[°]. In 2a, the O(1) atom is of the coordinated water molecule and the O(2) atom is of the coordinated ethanol molecule. The interatomic distances Co–O(1) = 2.157(2) and Co–O(2) = 2.184(2) Å; the bond angle O(1)–Co(1)–O(2) equals 167.03(7)[°].

In the crystal structure of coordination compounds 1 and 3, DMSO solvent molecules were found. Shortened S...S contacts with S atoms of the apical isothiocyanates were registered (S(1)...S(5) = 3.603, S(2)...S(3){1 + x, y, x} = 4.010 Å in 1 and 3.963 Å in 3), as well as intermolecular hydrogen bonds of the S=O...H–N type. In 2, intermolecular hydrogen bonds were formed between ClO₄[−] anions and solvate water molecules. As an example, the crystal packing of compounds 1 and 2 is shown in Figures 2 and 3, respectively.

**Figure 2.** Fragment of the crystal packing in 1.

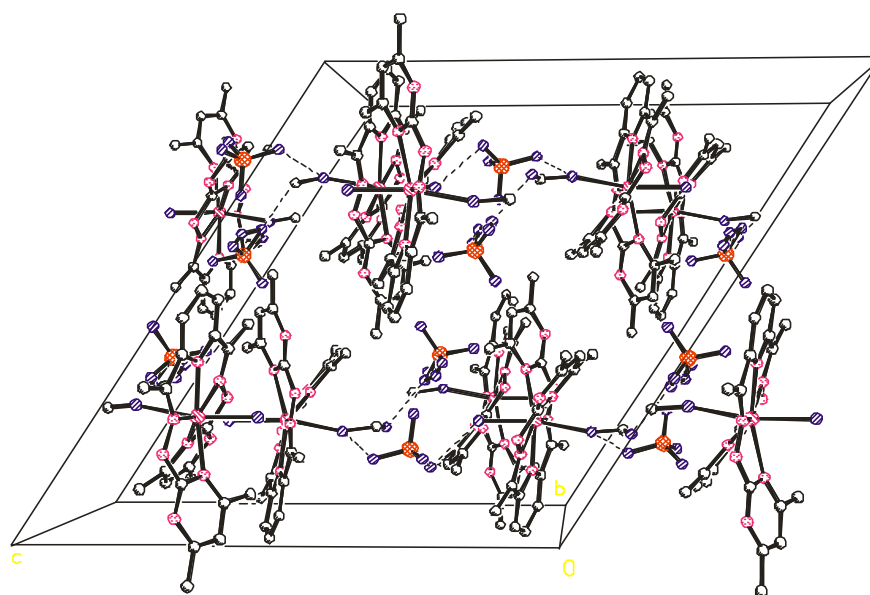


Figure 3. Fragment of the crystal packing in **2**.

In Table 2, the shortest intermolecular distances between paramagnetic metal centers Co ... Co and Fe ... Fe (M ... M contacts) are listed. In **2a**, due to the presence of the $[\text{CoCl}_4]^{2-}$ dianion, the distance between paramagnetic Co(II) centers is the shortest among all complexes.

Table 2. Shortest interatomic metal–metal (M ... M(1), Å) distances between mononuclear units and corresponding symmetry operations (#) in compounds 1–3 (M = Co (**1,2,2a**); Fe (**3**)).

	M ... M(1)#	#
1	7.886	$2 - x, -y, -z$
2	8.522	$-x, 1 - y, 1 - z$
	8.783	$1/2 - x, 1/2 + y, 3/2 - z$
2a	7.0735(5)	To Co ion of $[\text{CoCl}_4]^{2-}$ unit
3	7.795	$x, y, -1 + z$
	7.838	$2 - x, 1 + x - y, 1/3 + z$

In Figure 4, the molecular structure and atom-numbering scheme of compound **4** are presented.

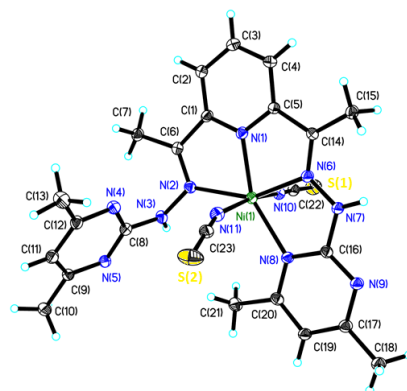


Figure 4. Molecular structure and atom-numbering scheme of compound **4**.

In contrast to compounds **1–3**, ligand **L** in compound **4** is tetradentate. The nitrogen atom N(4) is not coordinated to the nickel ion.

An uncoordinated hydrazinopyrimidine moiety is involved in a rather strong intermolecular hydrogen bond between the H(N3) and N(12) atoms of the acetonitrile molecule (Figure 5), with the following parameters: $d(\text{N}(12) \dots \text{H}(\text{N}3)) = 2.24$, $d(\text{N}(12) \dots \text{N}(3)) = 3.023 \text{ \AA}$, $\text{N}(12)\text{H}(\text{N}3)\text{N}(3)$ angle = 151.9° . The axial positions in the coordination polyhedron of the Ni(II) ion in compound **4** are filled with two NCS^- anions, similar to compounds **1** and **2** (interatomic distances $\text{Ni}(1) \dots \text{N}(11) = 2.028(4)$ and $\text{Ni}(1) \dots \text{N}(10) = 2.032(4) \text{ \AA}$). The bond angle $\text{N}(10)\text{--Ni}(1)\text{--N}(11)$ is $168.93(15)$, and the isothiocyanate moieties are close to linear (angles $\text{N}(11)\text{C}(23)\text{S}(2) = 178.8(5)$ and $\text{N}(10)\text{C}(22)\text{S}(1) = 177.6(4)^\circ$). At the same time, the NiNC angles differ significantly, i.e., $\text{Ni}(1)\text{--N}(10)\text{--C}(22) = 178.2$, $\text{Ni}(1)\text{--N}(11)\text{--C}(23) = 162.1^\circ$. Such deviation of the $\text{Ni}(1)\text{--N}(11)\text{--C}(23)$ angle from linearity is probably caused by the requirements of the crystal packing. The sulfur atom S(2) participates in three close contacts— $\text{S}(2) \dots \text{H}(15\text{C}) \{1 - x, 1/2 + y, 1/2 - z\} = 2.81$, $\text{S}(2) \dots \text{H}(10\text{C}) \{-1/2 + x, 3/2 - y, 1 - z\} = 2.81$, and $\text{S}(2) \dots \text{H}(24\text{B}) \{3/2 - x, 1 - y, -1/2 + z\} = 2.96 \text{ \AA}$ —but the S(1) atom forms only one close contact $\text{S}(1) \dots \text{H}(7\text{B})$, with an interatomic distance of 2.99 \AA . Thus, the coordination number of the Ni ion in compound **4** is six, in contrast to the cobalt and iron compounds **1–3** where it is seven.

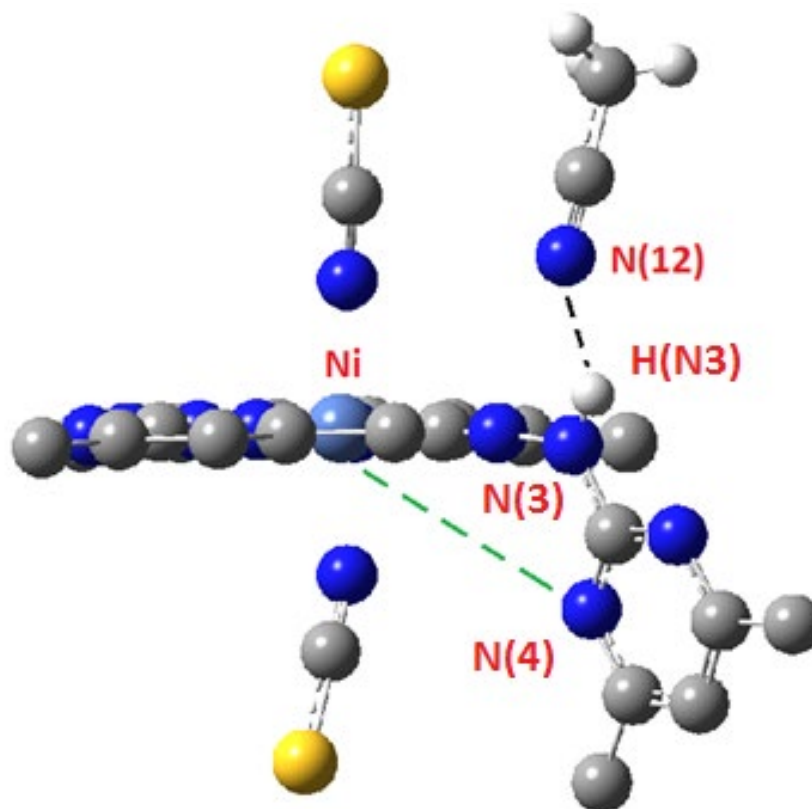


Figure 5. Intermolecular hydrogen bond between the nitrogen atom of the acetonitrile molecule and the hetarylhydrazone moiety of compound **4**.

In Figure 6, the fragment of the crystal packing of compound **4** is shown (the hydrogen atoms are omitted). The intermolecular hydrogen bond of the N-H ... N type has the following characteristics: $\text{H}(\text{N}7) \dots \text{N}(5\text{A}) \{3/2 - x, 1 - y, -1/2 + z\} = 2.20$, $\text{N}(7) \dots \text{N}(5) = 2.856 \text{ \AA}$, $\text{N}(7)\text{H}(\text{N}7)\text{N}(5) = 132.9^\circ$.

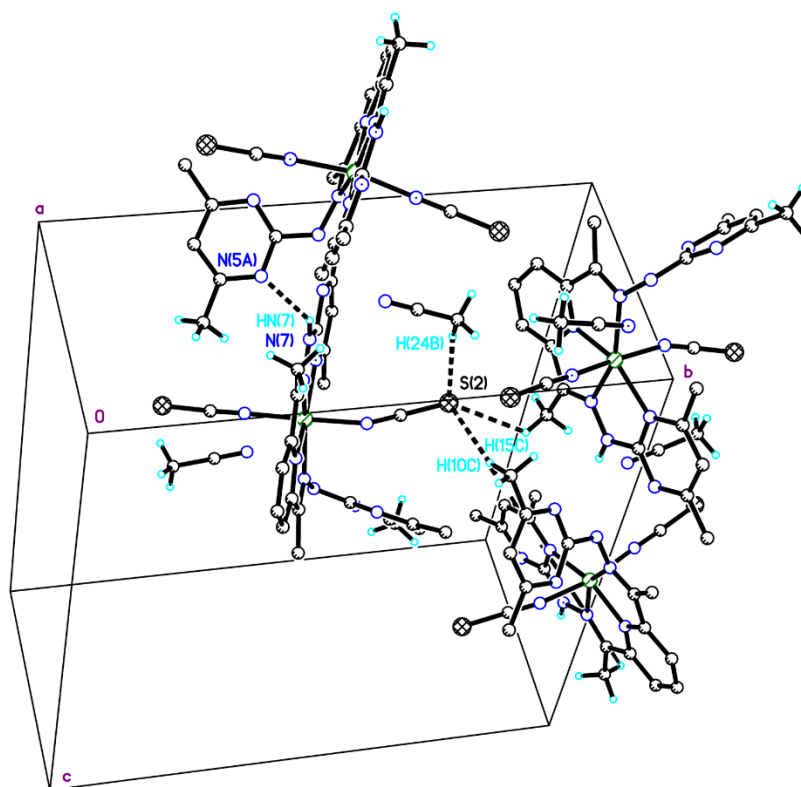


Figure 6. Fragment of the crystal packing of compound **4** (dotted lines indicate the the S(2) ... H contact and the N(7)-H(N7) ... N(5A) hydrogen bond) (a, b, c—crystallographic axes).

The shortest distance between Ni(II) paramagnetic centers in the crystal structure is 8.476 Å.

The coordination polyhedra of the metal coordination center are summarized in Figure 7, while the deviations of the donor nitrogen atoms of ligand L and metal center M from the equatorial plane (least-squares plane of atoms M, N(1), N(2), N(6)) are listed in Table 3.

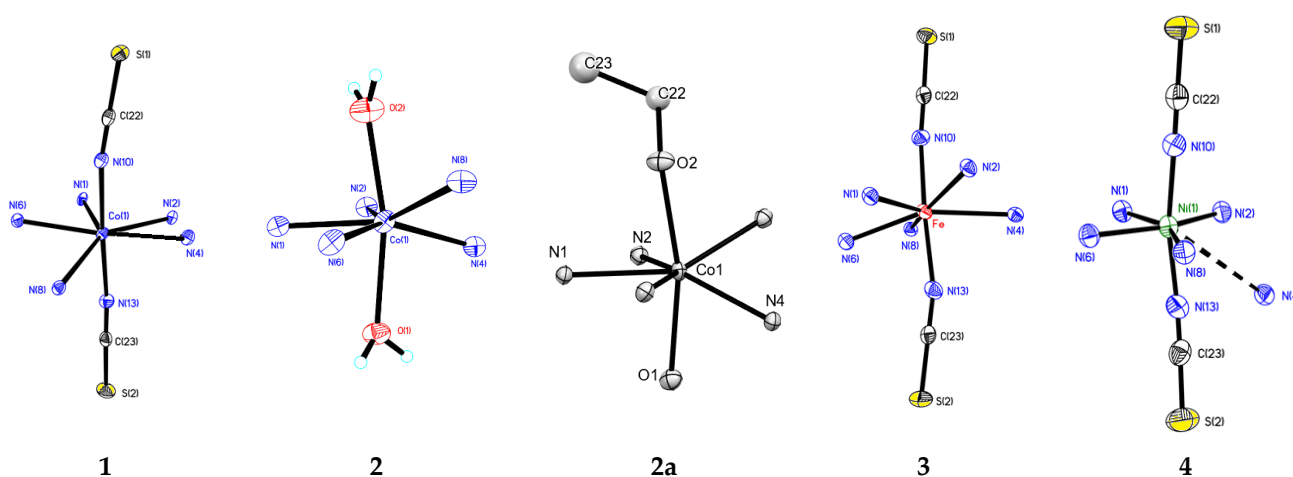


Figure 7. Coordination polyhedra in compounds **1–4**.

Table 3. Deviation of the donor atoms and the metal center M from the equatorial plane (least-squares plane of atoms M, N(1), N(2), N(6)), and value of the N(10)–M–N(11) angle.

Compound	M	N(4)	M	N(8)	N(10)–M–N(11) (for 1, 3, 4) O(1)–M–O(2) (for 2, 2a)
1	Co	−0.665	−0.132	0.561	177.4
2	Co	0.812	−0.007	−0.876	166.3
2a	Co	0.753	−0.005	−0.761	167.0
3	Fe	0.599	0.000	−0.599	173.7
4	Ni	2.388	0.059	0.09	168.9

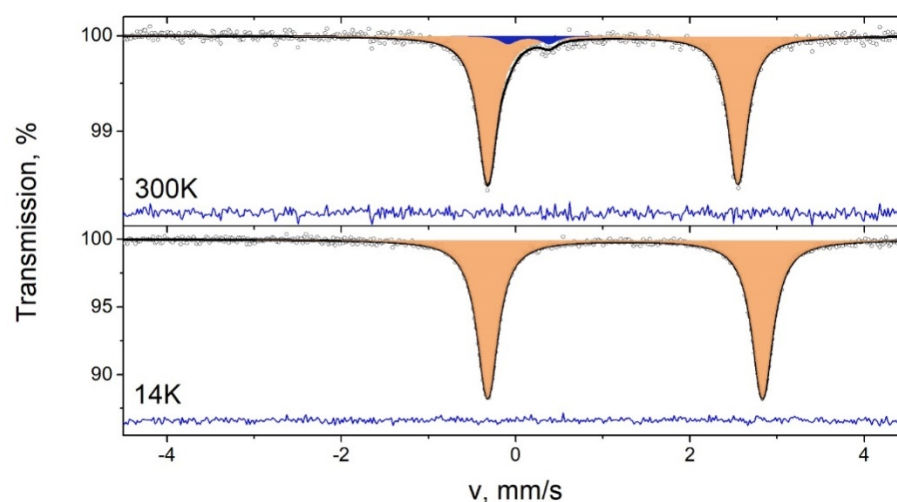
In polyhedron **4**, the N(6) and N(8) atoms have the least deviation from the plane formed by the N(1)N(2)Ni atoms; the N(4) atom that does not participate in the coordination has the largest deviation.

2.3. Mössbauer Spectroscopy of **3**

Mössbauer spectroscopy data were registered for complex **3** at 14 and 300 K (see Table 4 and Figure 8).

Table 4. Isomer shift (δ , mm/s), quadrupole splitting (Δ , mm/s), component area (A, %), linewidth (G, mm/s), and Pearson's criterion (χ^2) for the Mössbauer spectrum of **3** at 14 and 300 K.

T, K	Component	$\delta \pm 0.01$, mm/s	$\Delta \pm 0.01$, mm/s	A ± 1 , %	G ± 0.01 , mm/s	χ^2
300	D1	1.12	2.86	96	0.26	0.939
	D2	0.15	0.48	4	0.23	
14	D1	1.26	3.16	100	0.29	1.014

**Figure 8.** Calculated Mössbauer spectra of **3** at 300 and 14 K (the blue-colored area is for the admixture phase).

At room temperature, in addition to the signal of the main phase (component D1), the signal of the admixture (approximately 4%) is registered (component D2). The parameters of the admixture signal (component D2) are characteristic of iron in the Fe³⁺ state and a tetrahedral coordination environment, and this is probably observed due to the trace amounts of iron present in the Mylar window of the cryostat. At 14 K, the main signal has high intensity, and the admixture signal is not observed.

The isomer shift and the position of the quadrupole splitting of the signal are typical of the high-spin 2+ oxidation state at both temperatures.

2.4. DC Magnetic Properties

The magnetic properties of cobalt(II) complexes **1**, **2**, and **2a** were investigated under a 5000 Oe DC magnetic field in the 2–300 K temperature range. The temperature dependence of the molar magnetic susceptibility χ_M in the form $\chi_M T$ vs. T , along with the magnetization vs. field at 2, 4, and 6 K (insets) for these complexes, is presented in Figure 9.

Table 5. Spin-Hamiltonian best-fit parameters found from approximations of the DC magnetic properties of complexes 1–4.

Parameter	1	2	2a	3	4
	Value				
g_x	2.24(1) ^a	2.44(1)	2.29(2) ^b	2.38(1) ^c	2.22(1) ^a
g_y	-	2.34(2)		2.15(1)	
g_z	2.22(1)	2.02(1)	2.11(4)	2.54(2)	
D, cm^{-1}	13.7(1)	11.5(1)	20(1)	5.3(3)	-14.5(1)
E, cm^{-1}	2.5(1)	2.0(1)	-	-	0.7(1)
zJ, cm^{-1}	-0.04(1)	-0.05(1)	-0.07	-	-

^a $g_x = g_y$ for **1** and $g_x = g_y = g_z = g_{\text{iso}}$ for **4**. ^b Values in this column are assigned to the coordination unit $[\text{CoL}(\text{H}_2\text{O})(\text{EtOH})]$ of **2a** ($g_x = g_y$). ^c Values in this column are assigned to $[\text{CoCl}_4]^{2-}$ of **2a** ($g_x = g_y = g_z = g_{\text{iso}}$).

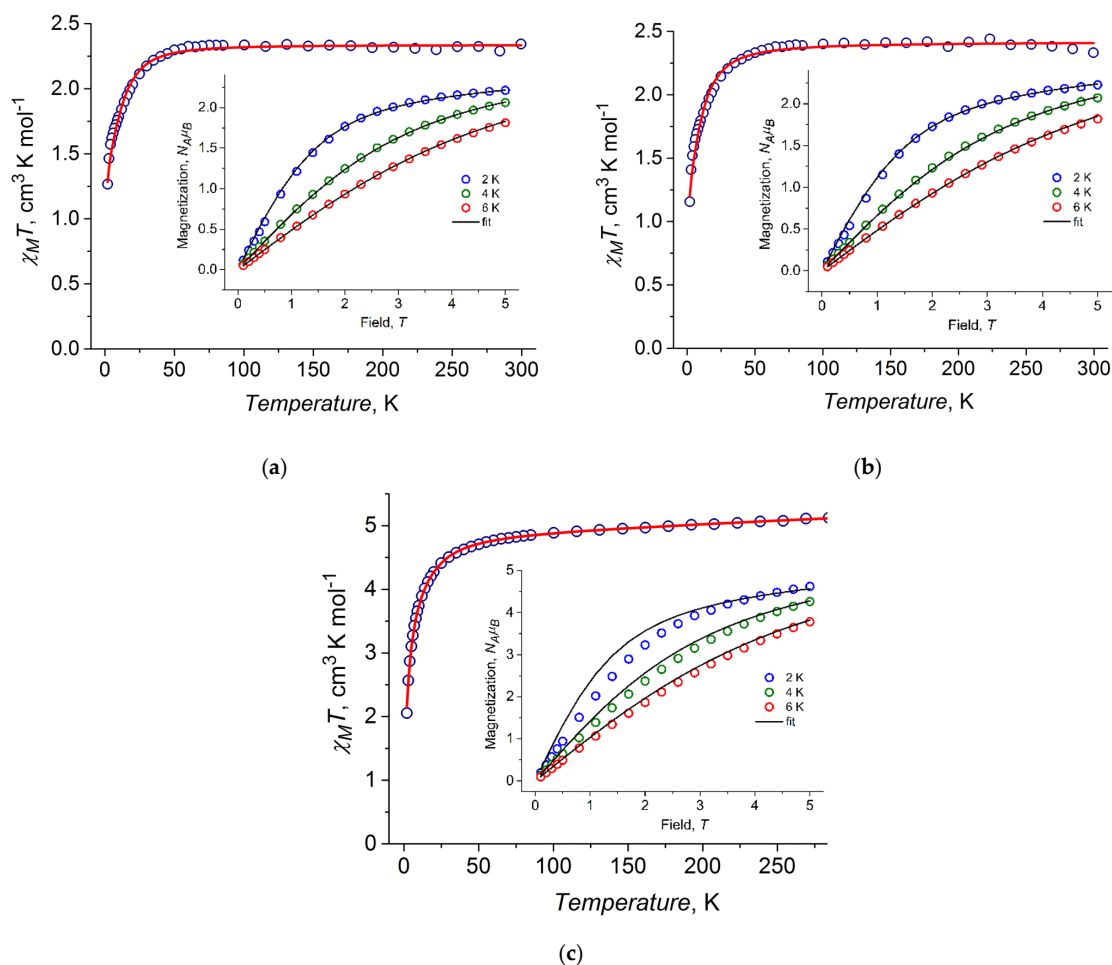


Figure 9. Temperature dependence of $\chi_M T$ for **1** (a), **2** (b), and **2a** (c) recorded at $H = 5000$ Oe (open circles). Inset: Magnetization vs. field for **1**, **2**, and **2a** measured at $T = 2, 4,$ and 6 K. Theoretical curves (solid lines) are calculated within the best-fit parameters listed in Table 5.

In the case of Co(II) compounds, the experimental $\chi_M T$ values at 300 K (2.34, 2.33, and 5.14 cm³/mol K for **1**, **2**, and **2a**, respectively; Figure 9a–c) are much higher than the spin-only value 1.875 cm³·K·mol^{−1} for the single paramagnetic centers with $S = 3/2$ and $g = 2$ (for **1** and **2**, respectively), and much higher than the ~3.75 cm³·K·mol^{−1} for two non-interacting Co(II) ions (for **2a**), indicating the presence of the unquenched orbital angular momentum contribution to the total magnetic momentum for all compounds. The $\chi_M T$ values are reduced to 1.27, 1.16, and 2.04 cm³·K mol^{−1} for **1**, **2**, and **2a**, respectively, when the temperature decreases from 300 K to 2 K. This low-temperature decrease in the $\chi_M T$ value can be attributed to the single-ion anisotropy associated with the zero-field splitting (ZFS) and antiferromagnetic intermolecular interactions between complexes in the crystal structure. Magnetization as a function of the magnetic field measured at $T = 2$ K is almost saturated at 5 T, reaching ca. 2.21 and 2.23 N_Aμ_B for **1** and **2**, respectively (insets in Figure 9), which is significantly lower than the value of 3 N_Aμ_B corresponding to the spin $S = 3/2$ ground state with $g = 2$. Moreover, the value of 4.51 N_Aμ_B observed at 2 K for **2a** is lower than the expected value for two non-interacting pure spin ions. Such behavior also indicates the presence of significant magnetic anisotropy in all complexes. To describe the DC magnetic properties, the following zero-field splitting (ZFS) spin Hamiltonian was used for **1** and **2**:

$$\hat{H} = D \left[\hat{S}_z^2 - \frac{1}{3} S(S+1) \right] + E \left(\hat{S}_x^2 - \hat{S}_y^2 \right) + \mu_B (B_X g_X \hat{S}_X + B_Y g_Y \hat{S}_Y + B_Z g_Z \hat{S}_Z) \quad (1)$$

The best-fit parameters for compounds **1–4** are shown in Table 5. To describe the DC magnetic properties of **2a**, one must take into account the presence of two paramagnetic centers with different local environments and, thus, employ the following modified ZFS spin Hamiltonian:

$$\hat{H} = \sum_i D_i \left[\hat{S}_z^2(i) - \frac{1}{3} S(S+1) \right] + \mu_B \sum_i [B_X g_{iX} \hat{S}_X(i) + B_Y g_{iY} \hat{S}_Y(i) + B_Z g_{iZ} \hat{S}_Z(i)], \quad (2)$$

where $S = 3/2$ is the spin of each of the two Co(II) ions, while D_1 and D_2 are axial ZFS parameters for each of the Co(II) ions. For the paramagnetic center Co1 in the tetrahedral [CoCl₄]^{2−} dianion, the isotropic g -factor was considered, while for the heptacoordinated Co2 in [CoL(H₂O)₂]²⁺, the unit components of g_i ($i = x, y, \text{ or } z$) were varied independently. The sets of the best-fit parameters are shown in Table 5. In addition to these parameters, the temperature-independent paramagnetic contribution $\chi_{tip} = 1.1 \times 10^{-4}$ cm³·mol^{−1} was added for the correct description of the experimental susceptibility data. To correctly reproduce the low-temperature susceptibility data measured for complexes **1**, **2**, and **2a**, weak antiferromagnetic intermolecular exchange was taken into account.

All of the Co(II) compounds show easy plane-type magnetic anisotropy, with a moderate positive value of the D parameter and rather low rhombicity.

The magnetic behavior of the iron(II) complex **3** was investigated under a 1000 Oe DC magnetic field in the 2–300 K temperature range. Figure 10 shows the temperature dependence of $\chi_M T$ measured for complex **3**, along with the field dependences of magnetization at 2, 3, 4, 5.5, and 10 K (insets). Description of the DC magnetic properties was also performed with the spin Hamiltonian described in Equation (1). The best-fit parameters for compound **3** are shown in Table 5.

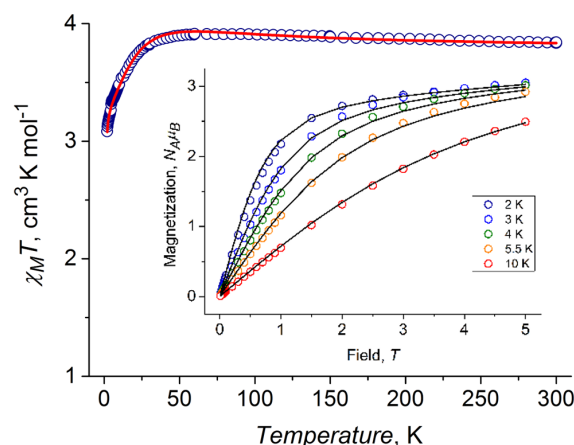


Figure 10. Temperature dependence of $\chi_M T$ for **3** measured under a 1000 Oe magnetic field (open circles). Inset: Magnetization vs. field for **3** measured at $T = 2, 3, 4, 5.5,$ and 10 K. The theoretical curves (solid lines) were calculated with the parameters shown in Table 5.

It can be seen that in contrast to the cobalt complexes, the iron(II) compound (**3**) shows easy axis-type magnetic anisotropy with a moderate negative value ($D = -14.5(1) \text{ cm}^{-1}$) and very low rhombicity ($E = 0.7(1) \text{ cm}^{-1}$).

The magnetic behavior of the nickel(II) complex **4** was investigated under a 5000 Oe DC magnetic field in the 2–300 K temperature range. The temperature dependence $\chi_M T$ measured for **4** is shown in Figure 11, along with the magnetization vs. field curves at 2, 3, and 5 K (insets). The description of the DC magnetic properties was also based on the spin Hamiltonian described in Equation (1). The best-fit parameters for compound **4** are shown in Table 5.

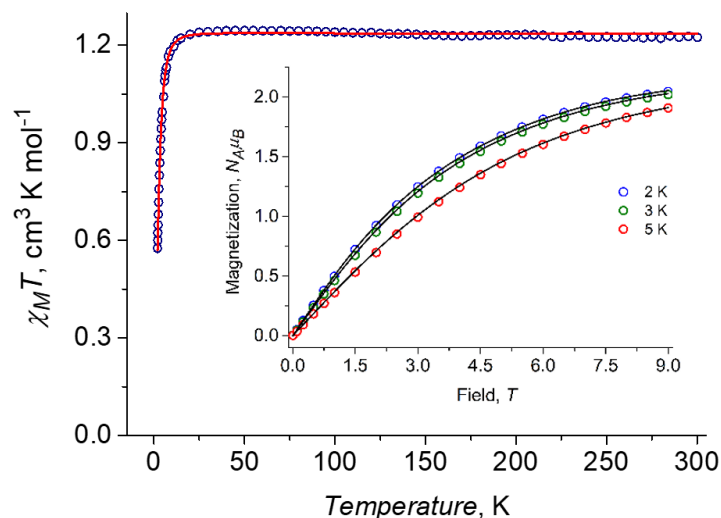


Figure 11. Temperature dependence $\chi_M T$ for **4** measured under a 5000 Oe magnetic field (open circles). Inset: Magnetization vs. field for **4** measured at $T = 2, 3,$ and 5 K. The theoretical curves (solid lines) were calculated with the optimal set of parameters (Table 5).

The observed best-fit values indicate that the nickel(II) compound exhibits rather weak easy plane-type magnetic anisotropy.

2.5. Computational Results

For all of the compounds, the electronic structure was studied with the CASSCF and NEVPT2 approaches (detailed descriptions of the computational methods are provided in the Supplementary Materials). The calculated principal components of the g-tensor and the values of the axial and rhombic anisotropy parameters are shown in Table 6. The calculated

and experimental values of the axial and rhombic anisotropy parameters are in fairly good agreement, except for compound **2**, for which the calculated D value is noticeably greater than the experimental one.

Table 6. Calculated (CASSCF and CASSCF + NEVPT2 level of theory) parameters of the effective spin Hamiltonian (D - and g -tensors) for complexes **1**–**4**.

Parameter	1	2	2a	3	4
	Value				
g_x	2.276/2.280	2.351/2.254	2.330/2.257	1.975/2.414	2.233/2.175
g_y	2.348/2.326	2.328/2.271	2.368/2.286	2.043/2.054	2.310/2.233
g_z	2.427/2.213	2.126/2.099	2.127/2.099	2.476/1.991	2.319/2.238
D, cm^{-1}	12.61/11.28	22.2/18.7	23.5/19.9	−22.10/−18.04	11.53/8.10
E, cm^{-1}	2.83/1.76	1.33/1.08	1.73/1.35	0.43/0.54	0.07/0.40
	23.4	37.5	40.2		

This may be due to the disordered structure of one of the axial positions in the Co coordination polyhedron (coordination of 75% water and 25% methanol molecules), while the magnetic anisotropy calculation was performed for the diaqua coordination unit. The calculated D value for **2a** is the closest to the experimental one and is higher than that of the other compounds, so heteroleptic substitution of the apical positions favors greater magnetic anisotropy.

For $[\text{CoCl}_4]^{2-}$ at the NEVPT2 level of theory and with nuclei coordinates taken from diffraction experiments, the calculated D value is 4.85 cm^{-1} . This supports the experimental fitting of the magnetic susceptibility in the DC field for the **2a** heterospin system.

2.6. Dynamic Magnetic Properties (AC Susceptibility)

In the $H_{\text{DC}} = 0$ magnetic field, the out-of-phase signal for complexes **1** and **2** is absent at 2 K for AC frequencies in the range of 10 Hz to 10 kHz (Figure S2, Supplementary Materials). At applied non-zero H_{DC} fields up to 5000 Oe, the significant out-of-phase signals on the $\chi''(\nu)$ dependence are observed. The optimal value of the DC field (at which the relaxation rate is the smallest) was selected as 1500 Oe for both complexes (Figure S2, Supplementary Materials).

The frequency dependences of the in-phase and out-of-phase components of the AC magnetic susceptibility for complexes **1** and **2** taken under a 1500 Oe field are shown in Figure 12.

The corresponding $\chi''(\nu)$ isotherms were approximated by using the two- and one-component generalized Debye models for complexes **1** and **2**, respectively. The resulting temperature dependences of relaxation time τ vs. $1/T$ are shown in Figure 13. The overall nonlinear course of these dependences evidences the contribution of non-Orbach magnetization relaxation mechanisms in both cases. One possible reason for the two-channel character of relaxation in complex **1** is the formation of domains (i.e., dimers or chains and blocks) through intermolecular interactions at low temperatures (<3 K), which is quite common for mononuclear hexacoordinated Co(II) complexes [40–45]. With increasing temperature, these supramolecular structures are fragmented into mononuclear units referring to only one relaxation channel. Indeed, the structures of **1** and **2** differ considerably. In **1**, all coordination M–N bonds in the complex are longer than in **2** (Table 1), due to the steric interactions of the atoms of the coordination center with bulkier apical substituents in **1** than in **2**. The shortening of the M–N bonds in **2** causes stronger distortion of the coordination plane as compared to **1**. DMSO molecules in the crystalline structure of **1** bind the molecules of the complex into the three-dimensional skeleton due to the S...S interactions and O...H(N) hydrogen bonds, with intermolecular Co...Co distances much shorter than in the crystalline structure of **2** (Table 2).

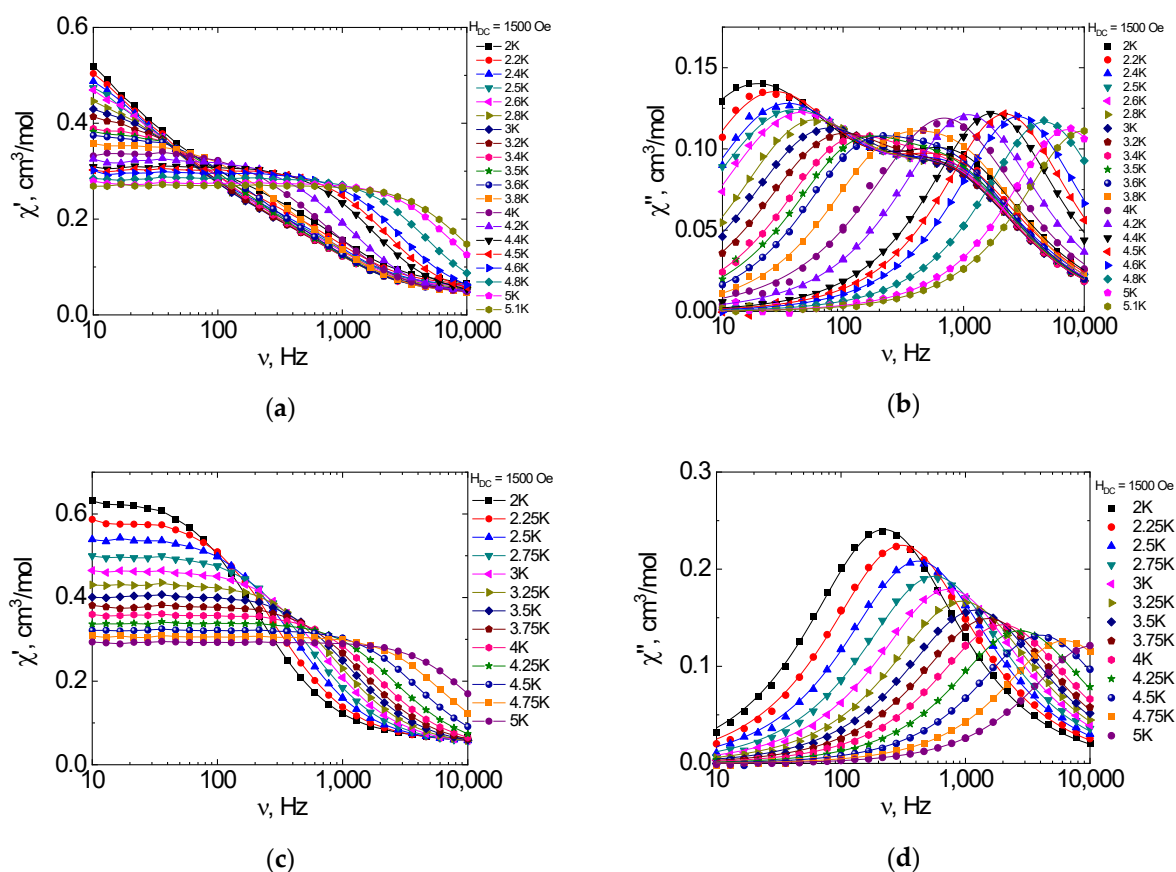


Figure 12. Frequency dependences of the in-phase χ' (a,c) and out-of-phase χ'' (b,d) AC susceptibility χ_M at different temperatures and $H_{DC} = 1500$ Oe for **1** (a,b) and **2** (c,d).

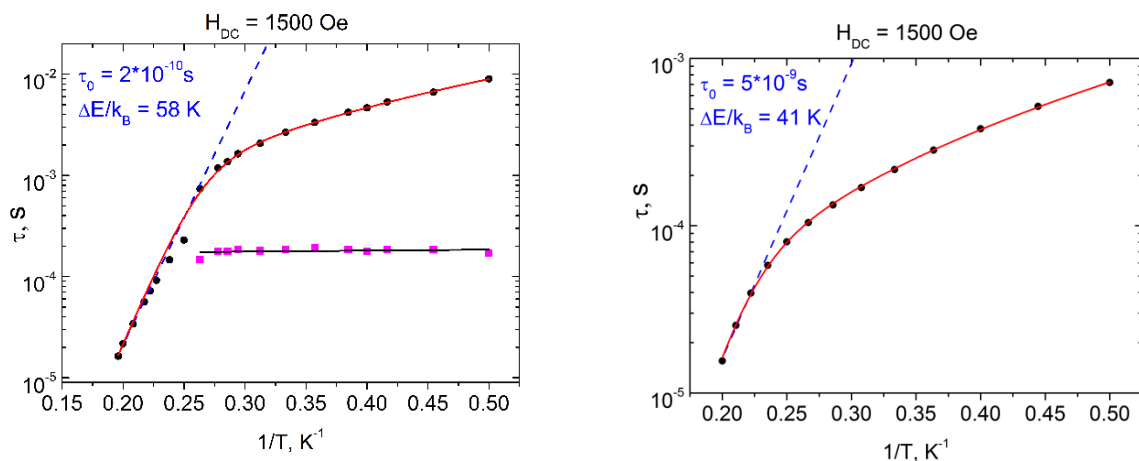


Figure 13. Relaxation time versus $1/T$ for **1** (left) and **2** (right) under an applied magnetic field of $H_{DC} = 1500$ Oe. Black circles and pink squares indicate low- and high-frequency peaks on $\chi''(\nu)$. The data were obtained by approximating the frequency dependences of the dynamic magnetic susceptibility using the two-component (1) and one-component (2) generalized Debye models. The blue line is the approximation of high-temperature data by the Arrhenius equation. The red line is the approximation of the entire data range by the combination of the Orbach and Raman relaxation mechanisms. The approximation of the second process by the QTM is shown by the black line.

In the high-temperature range—i.e., 3.8–5 K and 4.5–5 K for **1** and **2**, respectively—the $\tau(1/T)$ dependences are fairly well-described by the Arrhenius equation ($\tau = \tau_0 \cdot \exp\{\Delta_{\text{eff}}/kT\}$). Such an approximation affords the following sets of relaxation parameters: $\Delta_{\text{eff}}/k_B = 58$

and 41 K, $\tau_0 = 2 \times 10^{-10}$ and 5×10^{-9} s, for **1** and **2**, respectively. The best fit of the entire τ vs. $1/T$ dependence for **1** and **2** was achieved using a combination of Raman ($\tau^{-1} = CT^n$) and Orbach ($\tau = \tau_0 \cdot \exp\{\Delta_{\text{eff}}/kT\}$) mechanisms with the set of parameters listed in Table 7. The second relaxation process observed in **1** is temperature-independent and can be assigned to the mechanism of quantum tunneling of magnetization (QTM) with $\tau_{\text{QTM}} = 1.6(2) \times 10^{-4}$ s (pink squares and black line in the left panel of Figure 13).

Table 7. Parameters for the magnetic relaxation of complexes **1** and **2** obtained by fitting of the experimental relaxation times.

Complex	1	2
$\Delta_{\text{eff}}/k_B, \text{K}$	65(1)	60(1)
τ_0, s	$5.0(5) \times 10^{-11}$	$1.5(1) \times 10^{-10}$
$C, \text{s}^{-1}\text{K}^{-n}$	14.8(4)	182(3)
n	2.92(3)	2.93(2)
R^2	0.999	0.999

The cobalt (**2a**), iron (**3**), and nickel (**4**) compounds do not show dynamic magnetic properties (AC) in zero and applied DC fields up to 1T.

3. Materials and Methods

2-Hydrazinyl-4,6-dimethylpyrimidine was synthesized according to the method described in [46]. All other reagents and solvents were purchased from commercial sources and used without further purification. The ^1H NMR spectra were recorded in DMSO- d_6 using a 600 MHz Bruker Avance 600 spectrometer. The infrared spectra of solid samples were recorded using a Varian Scimitar 1000 FTIR spectrometer in the range of 400–4000 cm^{-1} . Microanalysis of C, H, and N was performed using a PerkinElmer 240C Analyzer. Metal contents were analyzed gravimetrically after pyrolysis of the coordination compounds. The powder XRD patterns for **1**, **2**, **2a**, **3**, and **4** were recorded on an Aeris diffractometer (Malvern PANalytical B.V., EA Almelo, Netherlands). The powder XRD measurements showed that all of the polycrystalline samples were monophasic crystalline materials corresponding to the single-crystal data (Figure S3).

The Mössbauer spectra of Fe(II) complex **3** were measured using an MS1104Em Mössbauer spectrometer in the temperature range of 14–300 K. The sample was cooled in a CCS-850 helium cryostat (Janis Res. Inc., Woburn, MA, USA). The ^{57}Co in the rhodium matrix was used as the γ -ray source. The experimental spectra were fitted using SpectrRelax software [47]. The isomer shifts were calculated with respect to the metallic α -Fe.

3.1. Synthesis of 2,6-bis(1-(2-(4,6-dimethylpyrimidin-2-yl)hydrazineylidene)ethyl)pyridine (**L**)

A hot solution of 2,6-diacetylpyridine (0.29 g, 1.8 mmol) in isopropanol (3 mL) was added to a boiling solution of 2-hydrazinyl-4,6-dimethylpyrimidine (0.5 g, 3.6 mol) in isopropanol (10 mL). Acetic acid (three drops) was then added, and the solution was refluxed for 6 h. After cooling, a yellow crystalline precipitate was formed and collected by filtration. The solid was washed with isopropanol and recrystallized from acetonitrile.

Yield: 0.53 g (73%). m.p. = 185 °C. Anal. Calcd for $\text{C}_{21}\text{H}_{25}\text{N}_9$: C, 62.51; H, 6.24; N, 31.24%; Found: C, 62.71; H, 6.35; N, 31.19%. (Anal. Calcd: Analysis calculated)

IR (cm^{-1}): 3364 (NH, m), 1592 (C=N, s), 1567 (C=N, s), 1556 (s), 1538 (m), 1519 (m), 1302 (m), 1261 (w), 1222 (w), 1179 (m), 1164 (m), 1150 (s), 1113 (w), 1085 (w), 1028 (w), 993 (w), 945 (w), 856 (m), 820 (m), 784 (m), 743 (w), 721 (w).

^1H NMR (DMSO- d_6 , 600 MHz), δ , ppm (J, Hz): 10.01 (2H, s, NH), 8.01 (2H, d, $J = 7.86$ Hz, H^3_{Py} , H^5_{Py}), 7.83 (1H, t, $J = 7.92$ Hz, H^4_{Py}), 6.66 (2H, s, $\text{H}_{\text{pyrimidine}}$), 2.44 (6H, s, CH_3), 2.32 (12H, s, CH_3).

3.2. Synthesis of $[CoL(NCS)_2] \cdot 3DMSO$ (1)

A hot solution of $Co(ClO_4)_2 \cdot 6H_2O$ (0.15 g, 0.4 mmol) in methanol (3 mL) was added to a boiling solution of L (0.16 g, 0.4 mmol) in methanol (10 mL). After 5 min, solid KSCN (0.078 g, 0.8 mmol) was added to the reddish-brown solution. A crystalline precipitate immediately formed. The reaction mixture was refluxed for 3 h. The precipitate was filtered off and recrystallized from a mixture of DMSO and methanol (2:1). Dark red single crystals suitable for X-ray diffraction (XRD) experiments were obtained by slow evaporation of the saturated DMSO–methanol mixture.

Yield: 0.150 g (46%). m.p. > 260 °C. Anal. Calcd for $C_{29}H_{43}CoN_{11}O_3S_5$: C, 42.85; H, 5.33; Co, 7.25, N, 18.95, O, 5.9; S, 19.72%. Found: C, 42.81; H, 5.39; Co, 7.29; N, 19.01; S, 19.83%.

IR (cm^{-1}): 3211 (NH, w), 3138 (NH, w), 2082 (NCS^- , s), 2066 (NCS^- , s), 1651 (C=N, s), 1595 (C=N, s), 1537 (s), 1434 (s), 1377 (m), 1356 (m), 1339 (s), 1280 (w), 1251 (m), 1205 (m), 1188 (m), 1176 (m), 1134 (m), 1100 (w), 1061 (w), 1030 (w), 997 (w), 954 (m), 838 (m), 809 (w), 787 (m), 746 (w), 684 (w), 661 (w), 629 (m), 603 (w), 543 (w), 534 (w), 453 (w), 422 (w), 405 (w).

3.3. Synthesis of $[CoL(H_2O)_2](ClO_4)_2 \cdot H_2O$ (2)

A hot solution of $Co(ClO_4)_2 \cdot 6H_2O$ (0.15 g, 0.4 mmol) in methanol (2 mL) was added to a boiling solution of L (0.16 g, 0.4 mmol) in methanol (8 mL). The solution was refluxed for 5 h and left undisturbed. After five days, brown crystals of Co(II) complexes arose from the solution.

Yield: 0.17 g (59%). m.p. > 260 °C. Anal. Calcd for $C_{21}H_{31}Cl_2CoN_9O_{11}$: C, 35.26; H, 4.37; Cl, 9.91, Co, 8.24, N, 17.62, O, 24.6%; Found: C, 35.2; H, 4.07; Co, 8.3; N, 17.51%.

IR (cm^{-1}): 3470 (H_2O , w), 3281 (NH, w), 1606 (C=N, m), 1542 (C=N, m), 1423 (m), 1350 (m), 1275 (w), 1208 (m), 1181 (w), 1075 (ClO_4^- , s), 839 (w), 813 (w), 785 (w), 745 (w), 687 (w), 654 (w), 621 (s), 545 (w), 504 (w), 480 (m), 445 (m), 418 (m).

3.4. Synthesis of $[CoL(H_2O)(C_2H_5OH)][CoCl_4] \cdot 2H_2O$ (2a)

A hot solution of $CoCl_2 \cdot 6H_2O$ (0.095 g, 0.4 mmol) in methanol (2 mL) was added to a boiling solution of L (0.16 g, 0.4 mmol) in methanol (8 mL). The solution was refluxed for 5 h. After a few days, brown crystals of Co(II) complexes arose from the solution. The precipitate was filtered off and recrystallized from ethanol.

Yield: 0.16 g (54%). mp > 260 °C. Anal. Calcd for $C_{23}H_{37}Cl_4Co_2N_9O_4$: C, 36.19; H, 4.89; Cl, 18.58, Co, 15.44, N, 16.52, O, 8.38%; Found: C, 36.3; H, 4.7; Co, 15.3; N, 16.3%.

IR (cm^{-1}): 3393 (H_2O , m), 3348 (C_2H_5OH , m), 3188 (NH, m), 1645 (C=N, s), 1602 (C=N, s), 1540 (s), 1428 (m), 1358 (m), 1276 (w), 1211 (m), 1183 (m), 1169 (m), 1140 (w), 1118 (w), 1093 (m), 1042 (w), 956 (w), 855 (w), 813 (w), 783 (m), 749 (m), 662 (w), 630 (w), 518 (m), 443 (m).

3.5. Synthesis of $[FeL(NCS)_2] \cdot DMSO$ (3)

A hot solution of $Fe(ClO_4)_2 \cdot 6H_2O$ (0.17 g, 0.47 mmol) in methanol (3 mL) was added to a boiling solution of L (0.19 g, 0.47 mmol) in methanol (10 mL). After 5 min, solid KSCN (0.096 g, 0.99 mmol) was added to the reddish-crimson solution. The solution turned dark gray, and a crystalline precipitate formed. The reaction mixture was refluxed for 1 h. The precipitate was filtered off and recrystallized from the mixture of DMSO and ethanol (2:1). After three days, dark gray crystals of Fe(II) complexes arose from the solution.

Yield: 0.250 g (81%). m.p. > 260 °C. Anal. Calcd for $C_{25}H_{31}FeN_{11}OS_3$: C, 45.94; H, 4.78; Fe, 8.54, N, 23.57, O, 2.45; S, 14.17%. Found: C, 46.1; H, 4.6; Fe, 8.3; N, 23.7; S, 13.9%.

IR (cm^{-1}): 3317 (NH, w), 2059 (NCS^- , s), 1596 (C=N, s), 1543 (C=N, m), 1434 (m), 1389 (w), 1344 (m), 1277 (w), 1228 (w), 1199 (m), 1178 (m), 1162 (m), 995 (m), 940 (m), 842 (w), 826 (w), 808 (m), 782 (m), 740 (w), 624 (s), 555 (w), 458 (m).

3.6. Synthesis of $[NiL(NCS)_2] \cdot CH_3CN$ (**4**)

A hot solution of $Ni(ClO_4)_2 \cdot 6H_2O$ (0.14 g, 0.38 mmol) in methanol (3 mL) was added to a boiling solution of **L** (0.15 g, 0.38 mmol) in methanol (10 mL). After 5 min, solid KSCN (0.074 g, 0.76 mmol) was added to the reddish/dark brown solution. A crystalline precipitate immediately formed. The reaction mixture was refluxed for 3 h. The precipitate was filtered off and recrystallized from CH_3CN . The next day, brown crystals of the Ni(II) complex arose from the solution.

Yield: 0.13 g (57%). m.p. > 260 °C. Anal. Calcd for $C_{25}H_{28}NiN_{12}S_2$: C, 48.48; H, 4.56; Ni, 9.48, N, 27.14; S, 10.35%. Found: C, 48.6; H, 4.9; Ni, 9.1; N, 27.3; S, 10.4%.

IR (cm^{-1}): 3315 (NH, m), 3157 (NH, w), 2092 (NCS, s), 2855 (NCS^- , s), 2092 (CN^- , s), 1602 (C=N, s), 1590 (C=N, s), 1556 (s), 1462 (s), 1455 (s), 1365 (s), 1347 (m), 1273 (m), 1235 (m), 1216 (w), 1192 (w), 1178 (m), 1176 (m), 1131 (w), 1116 (w), 1091 (w), 1007 (w), 994 (w), 849 (w), 827 (w), 807 (m), 783 (w), 739 (w), 722 (w), 670 (w), 615 (w), 573 (w), 562 (w), 544 (m).

3.7. Single-Crystal X-ray Diffraction Study

Diffraction data for single crystals of **1–3** were collected using an Agilent XCalibur CCD diffractometer with an EOS detector (Agilent Technologies UK Ltd., Yarnton, Oxfordshire, England), using graphite-monochromated Mo K_α radiation ($\lambda = 0.71073 \text{ \AA}$). Data collection, determination, and refinement of the unit cell were performed with the specialized CrysAlis PRO software [48]. The single-crystal X-ray diffraction data were obtained at 100.0(1) K. The structures were solved by direct methods. Full-matrix refinement of the position and thermal parameters of the non-hydrogen atoms was performed isotropically, followed by anisotropic refinement by the least-squares method. All calculations were performed with the SHELXTL set of programs [49].

The single-crystal X-ray diffraction dataset for the single crystals of **4** were collected at the “Belok/XSA” beamline [50,51] of the Kurchatov synchrotron radiation source (National Research Centre “Kurchatov Institute”), equipped with a Rayonix SX165 CCD detector ($\lambda = 0.79475 \text{ \AA}$, φ -scanning technique with a step of 1°). The intensities were integrated, absorption corrections were applied, and the unit cell parameters were determined using the XDS program package [52]. The structure was solved by direct methods with SHELXT software [53]. The structural model was investigated and refined by using Olex2 software [54] with the full-matrix least-squares method on F^2 with anisotropic displacement, and the hydrogen atoms were placed according to the geometry and residual electron density peaks.

For full details of the X-ray diffraction experiments and the refinement procedures for compounds **1–4**, see Table S3 (Supplementary Materials). Selected bond lengths and angles are given in Table S2 (Supplementary Materials). CIF files containing full information for the studied structures have been deposited at the Cambridge Crystallographic Data Center (deposition CCDC numbers are given in Table S3 of the Supplementary Materials) and can be requested free of charge from the following website: www.ccdc.cam.ac.uk/data_request/cif (accessed on 3 October 2022).

3.8. Magnetic Measurements

Magnetic susceptibility measurements were performed using a Quantum Design PPMS-9 susceptometer. DC magnetic susceptibility measurements for Co (**1**, **2**, **2a**) and Ni (**4**) compounds were performed under a 5000 Oe magnetic field, while for the Fe complex (**3**) a 1000 Oe magnetic field was applied. The measurements were performed in the 2–300 K temperature range. For AC susceptibility measurements of all of the samples, oscillating AC magnetic fields of 5, 3, and 1 Oe were applied within frequency ranges of 10–100, 100–1000, and 1000–10,000 Hz, respectively. These settings allowed us to avoid sample heating at low temperatures (which may occur when the modulation amplitudes and frequency are high) as well as to obtain the best signal-to-noise ratio. All of the magnetic measurements were performed on polycrystalline samples sealed in polyethylene bags

and covered with mineral oil to prevent the field-induced orientation of crystallites. The paramagnetic components of the magnetic susceptibility χ were determined considering both the diamagnetic contribution evaluated from Pascal's constants and the contributions of the sample holder and mineral oil.

3.9. Computational Details

Theoretical calculations of the electronic structure for complexes **1–4** were performed using post-Hartree–Fock multi-reference wave function (WF) approach based on state-averaged complete active space self-consistent field calculations (SA-CASSCF) [55–58], followed by N-electron valence second-order perturbation theory (NEVPT2) [58–61]. Scalar relativistic effects were accounted for while using a standard second-order Douglas–Kroll–Hess (DKH) procedure [62]. For calculations, the segmented all-electron relativistically contracted version [63] of Ahlrichs polarized triple- ζ basis set, def2-TZVP [64–66], was used for all atoms. To improve the calculation time, the resolution of the identity approximation with corresponding correlation fitting of the basis set [67] was employed. Spin–orbit effects were included using the quasi-degenerate perturbation theory (QDPT) [68].

The CASSCF(n , 5) active space was constructed from 5 MOs with predominant contributions of 3d-AOs from the metal center and the number of electrons, corresponding to a metal ion electronic configuration ($n = 6$ for Fe(II), 7 for Co(II) and 8 for Ni(II) compounds). All possible multiplet states arising from the corresponding d^n configuration were included in the WF expansion in all cases.

Nuclei coordinates of non-hydrogen atoms were taken from diffraction experimental data, positions of hydrogen atoms were optimized employing density functional theory with the BP86 functional and Ahlrichs polarized basis set def2-TZVP [10–12] (optimized nuclei coordinates are listed in Table S4 of the Supplementary Materials).

4. Conclusions

In summary, in the cases of Co(II) and Fe(II) ions, helical-like distortion of the coordinated pentadentate ligand **L** results in a decrease in the accessibility of axial coordination positions for large monodentate anions (e.g., chloride, bromide), while allowing coordination of NCS- and small solvent molecules (e.g., water, methanol). In the case of Ni(II) ions, a distorted octahedral coordination polyhedron is formed, in which **L** forms four coordination bonds with the metal atom, while one of the terminal pyrimidine fragment nitrogen atoms is uncoordinated due to the fragment rotation. Analysis of the magnetic properties revealed easy plane-type magnetic anisotropy for the cobalt and nickel compounds and easy axis-type magnetic anisotropy for the iron compound. The cobalt coordination compounds **1** and **2** showed SIM behavior under a 1500 Oe external magnetic field, with effective magnetization reversal barriers of 65(1) and 60(1) K for **1** and **2**, respectively. The combination of Orbach and Raman relaxation mechanisms proved to adequately describe the temperature dependences of relaxation times for **1** and **2**. Finally, neither at zero field nor under an applied DC field did the cobalt compound **2a**, the iron compound **3**, or the nickel compound **4** demonstrate slow magnetic relaxation.

Supplementary Materials: The following supporting information can be downloaded at: <https://www.mdpi.com/article/10.3390/magnetochemistry8110153/s1>, Table S1: Deviations from the ideal structure calculated using the SHAPE program [1] for several selected types of polyhedral* coordination, with coordination numbers of seven (**1–3**) and six (**4**) Table S2: Selected structural parameters for **1–4**; Table S3: Crystallographic data for **1–4**; Table S4: Optimized nuclei coordinates for **1–4** used for molecular modelling of the magnetic properties; Figure S1: Molecular structure of the reaction product of **L** with Co(II) bromide in methanol; Figure S2: Frequency dependences of the out-of-phase χ'' AC susceptibility χ_M for **1** (left) and **2** (right) under different applied magnetic fields (H_{DC}) and $T = 2$ K; Figure S3: Powder X-ray diffraction patterns of polycrystalline samples of **1** (a), **2** (b) **2a** (c), **3** (d), and **4** (e): experimental results (blue) and those calculated from single-crystal data.

Author Contributions: Conceptualization, I.N.S. and S.M.A.; Formal Analysis, I.N.S.; Funding Acquisition, S.M.A.; Investigation, Y.P.T., D.V.K., A.S.A., V.V.T., G.V.S., V.A.L., L.D.P., K.A.B., N.N.E., R.B.M. and S.P.K.; Methodology, A.V.P.; Resources, S.M.A.; Validation, D.V.K. and A.V.P.; Writing—Original Draft, D.V.K. and I.N.S.; Writing—Review and Editing, I.N.S. and S.M.A. All authors have read and agreed to the published version of the manuscript.

Funding: This research was financially supported by Southern Federal University (Y.P.T., A.S.A., V.A.L., L.D.P., S.P.K., I.N.S.). The work was performed with financial support from the Ministry of Science and Higher Education of RF (state assignment no AAAA-A19-119092390079-8) (D.V.K., V.V.T., G.V.S., R.B.M., A.V.P., S.M.A.).

Acknowledgments: Quantum chemical calculations were performed at the Joint Resource Centre “High-performance calculations” of SFedU. The research was partially performed using the equipment of the JRC PMR IGIC RAS.

Conflicts of Interest: The authors declare no conflict of interest.

References

1. Gomez-Coca, S.; Cremades, E.; Aliaga-Alcalde, N.; Ruiz, E. Mononuclear Single-Molecule Magnets: Tailoring the Magnetic Anisotropy of First-Row Transition-Metal Complexes. *J. Am. Chem. Soc.* **2013**, *135*, 7010–7018. [[CrossRef](#)] [[PubMed](#)]
2. Ruamps, R.; Batchelor, L.J.; Maurice, R.; Gogoi, N.; Jiménez-Lozano, P.; Guihéry, N.; de Graaf, C.; Barra, A.-L.; Sutter, J.-P.; Mallah, T. Origin of the Magnetic Anisotropy in Heptacoordinate NiII and CoII Complexes. *Chem. Eur. J.* **2013**, *19*, 950–956. [[CrossRef](#)] [[PubMed](#)]
3. Darmanović, D.; Shcherbakov, I.N.; Duboc, C.; Spasojević, V.; Hanžel, D.; Anđelković, K.; Radanović, D.; Turel, I.; Milenković, M.; Gruden, M.; et al. Combined Experimental and Theoretical Investigation of the Origin of Magnetic Anisotropy in Pentagonal Bipyramidal Isothiocyanato Co(II), Ni(II), and Fe(III) Complexes with Quaternary-Ammonium-Functionalized 2,6-Diacetylpyridine Bisacylhydrazone. *J. Phys. Chem. C* **2019**, *123*, 31142–31155. [[CrossRef](#)]
4. Gatteschi, D. Single molecule magnets: A new class of magnetic materials. *J. Alloys Compd.* **2001**, *317–318*, 8–12. [[CrossRef](#)]
5. Gatteschi, D.; Bogani, L.; Cornia, A.; Mannini, M.; Sorace, L.; Sessoli, R. Molecular magnetism, status and perspectives. *Solid State Sci.* **2008**, *10*, 1701–1709. [[CrossRef](#)]
6. Caneschi, A.; Gatteschi, D.; Sessoli, R.; Barra, A.L.; Brunel, L.C.; Guillot, M. Alternating current susceptibility, high field magnetization, and millimeter band EPR evidence for a ground $S = 10$ state in $[\text{Mn}12\text{O}12(\text{CH}_3\text{COO})_{16}(\text{H}_2\text{O})_4] \cdot 2\text{CH}_3\text{COOH} \cdot 4\text{H}_2\text{O}$. *J. Am. Chem. Soc.* **1991**, *113*, 5873–5874. [[CrossRef](#)]
7. Kahn, O. *Molecular Magnetism*; VCH Publishers: New York, NY, USA, 1993; p. 396.
8. Sessoli, R.; Gatteschi, D.; Caneschi, A.; Novak, M.A. Magnetic bistability in a metal-ion cluster. *Nature* **1993**, *365*, 141–143. [[CrossRef](#)]
9. Miller, J.S.; Gatteschi, D. Molecule-based magnets. *Chem. Soc. Rev.* **2011**, *40*, 3065–3066. [[CrossRef](#)]
10. Ferrando-Soria, J.; Vallejo, J.; Castellano, M.; Martínez-Lillo, J.; Pardo, E.; Cano, J.; Castro, I.; Lloret, F.; Ruiz-García, R.; Julve, M. Molecular magnetism, quo vadis? A historical perspective from a coordination chemist viewpoint. *Coord. Chem. Rev.* **2017**, *339*, 17–103. [[CrossRef](#)]
11. Lukov, V.V.; Kogan, V.A.; Levchenkov, S.I.; Shcherbakov, I.N.; Popov, L.D. Modern studies in the area of molecular magnets: State, problems, and prospects. *Russ. J. Coord. Chem.* **2015**, *41*, 1–15. [[CrossRef](#)]
12. Gatteschi, D.; Cornia, A.; Mannini, M.; Sessoli, R. Organizing and Addressing Magnetic Molecules. *Inorg. Chem.* **2009**, *48*, 3408–3419. [[CrossRef](#)] [[PubMed](#)]
13. Ritter, S.K. Single-Molecule Magnets Evolve. *Chem. Eng. News Arch.* **2004**, *82*, 29–32. [[CrossRef](#)]
14. Sanvito, S. Molecular spintronics. *Chem. Soc. Rev.* **2011**, *40*, 3336–3355. [[CrossRef](#)] [[PubMed](#)]
15. Bogani, L. Experiments on Molecular Magnets for Molecular Spintronics. In *Molecular Nanomagnets and Related Phenomena*; Gao, S., Ed.; Springer: Berlin/Heidelberg, Germany, 2015; pp. 331–381.
16. Winpenny, R.E.P. Quantum Information Processing Using Molecular Nanomagnets as Qubits. *Angew. Chem Int. Ed.* **2008**, *47*, 7992–7994. [[CrossRef](#)] [[PubMed](#)]
17. Troiani, F.; Affronte, M. Molecular spins for quantum information technologies. *Chem. Soc. Rev.* **2011**, *40*, 3119–3129. [[CrossRef](#)]
18. Leuenberger, M.N.; Loss, D. Quantum computing in molecular magnets. *Nature* **2001**, *410*, 789–793. [[CrossRef](#)] [[PubMed](#)]
19. Cornia, A.; Mannini, M.; Sainctavit, P.; Sessoli, R. Chemical strategies and characterization tools for the organization of single molecule magnets on surfaces. *Chem. Soc. Rev.* **2011**, *40*, 3076–3091. [[CrossRef](#)]
20. Miller, J.S. Magnetically ordered molecule-based materials. *Chem. Soc. Rev.* **2011**, *40*, 3266–3296. [[CrossRef](#)]
21. Jeon, I.-R.; Clerac, R. Controlled association of single-molecule magnets (SMMs) into coordination networks: Towards a new generation of magnetic materials. *Dalton Trans.* **2012**, *41*, 9569–9586. [[CrossRef](#)]
22. Coronado, E. Molecular magnetism: From chemical design to spin control in molecules, materials and devices. *Nat. Rev. Mater.* **2020**, *5*, 87–104. [[CrossRef](#)]

23. Frost, J.M.; Harriman, K.L.M.; Murugesu, M. The rise of 3-d single-ion magnets in molecular magnetism: Towards materials from molecules? *Chem. Sci.* **2016**, *7*, 2470–2491. [[CrossRef](#)] [[PubMed](#)]
24. Craig, G.A.; Murrie, M. 3d single-ion magnets. *Chem. Soc. Rev.* **2015**, *44*, 2135–2147. [[CrossRef](#)] [[PubMed](#)]
25. Cirera, J.; Ruiz, E.; Alvarez, S.; Neese, F.; Kortus, J. How to Build Molecules with Large Magnetic Anisotropy. *Chem. Eur. J.* **2009**, *15*, 4078–4087. [[CrossRef](#)]
26. Saber, M.R.; Singh, M.K.; Dunbar, K.R. Geometrical control of the magnetic anisotropy in six coordinate cobalt complexes. *Chem. Commun.* **2020**, *56*, 8492–8495. [[CrossRef](#)] [[PubMed](#)]
27. Meng, Y.-S.; Jiang, S.-D.; Wang, B.-W.; Gao, S. Understanding the Magnetic Anisotropy toward Single-Ion Magnets. *Acc. Chem. Res.* **2016**, *49*, 2381–2389. [[CrossRef](#)]
28. Bar, A.K.; Pichon, C.; Sutter, J.-P. Magnetic anisotropy in two- to eight-coordinated transition–metal complexes: Recent developments in molecular magnetism. *Coord. Chem. Rev.* **2016**, *308*, 346–380. [[CrossRef](#)]
29. Groom, C.R.; Bruno, I.J.; Lightfoot, M.P.; Ward, S.C. The Cambridge Structural Database. *Acta Crystallogr. Sect. B* **2016**, *72*, 171–179. [[CrossRef](#)]
30. Drahoš, B.; Čísařová, I.; Laguta, O.; Santana, V.T.; Neugebauer, P.; Herchel, R. Structural, magnetic, redox and theoretical characterization of seven-coordinate first-row transition metal complexes with a macrocyclic ligand containing two benzimidazolyl N-pendant arms. *Dalton Trans.* **2020**, *49*, 4425–4440. [[CrossRef](#)]
31. Antal, P.; Drahoš, B.; Herchel, R.; Trávníček, Z. Late First-Row Transition-Metal Complexes Containing a 2-Pyridylmethyl Pendant-Armed 15-Membered Macrocyclic Ligand. Field-Induced Slow Magnetic Relaxation in a Seven-Coordinate Cobalt(II) Compound. *Inorg. Chem.* **2016**, *55*, 5957–5972. [[CrossRef](#)]
32. Sutter, J.-P.; Béreau, V.; Jubault, V.; Bretosh, K.; Pichon, C.; Duhayon, C. Magnetic anisotropy of transition metal and lanthanide ions in pentagonal bipyramidal geometry. *Chem. Soc. Rev.* **2022**, *51*, 3280–3313. [[CrossRef](#)]
33. Huang, X.-C.; Zhou, C.; Shao, D.; Wang, X.-Y. Field-Induced Slow Magnetic Relaxation in Cobalt(II) Compounds with Pentagonal Bipyramid Geometry. *Inorg. Chem.* **2014**, *53*, 12671–12673. [[CrossRef](#)] [[PubMed](#)]
34. Shao, D.; Zhang, S.-L.; Shi, L.; Zhang, Y.-Q.; Wang, X.-Y. Probing the Effect of Axial Ligands on Easy-Plane Anisotropy of Pentagonal-Bipyramidal Cobalt(II) Single-Ion Magnets. *Inorg. Chem.* **2016**, *55*, 10859–10869. [[CrossRef](#)] [[PubMed](#)]
35. Yi, G.; Cui, H.; Zhang, C.; Zhao, W.; Chen, L.; Zhang, Y.-Q.; Chen, X.-T.; Song, Y.; Yuan, A. A capped trigonal prismatic cobalt(ii) complex as a structural archetype for single-ion magnets. *Dalton Trans.* **2020**, *49*, 2063–2067. [[CrossRef](#)] [[PubMed](#)]
36. Yi, G.; Zhang, C.; Zhao, W.; Cui, H.; Chen, L.; Wang, Z.; Chen, X.-T.; Yuan, A.; Liu, Y.-Z.; Ouyang, Z.-W. Structure, magnetic anisotropy and relaxation behavior of seven-coordinate Co(ii) single-ion magnets perturbed by counter-anions. *Dalton Trans.* **2020**, *49*, 7620–7627. [[CrossRef](#)] [[PubMed](#)]
37. Regueiro-Figueroa, M.; Lima, L.M.P.; Blanco, V.; Esteban-Gómez, D.; de Blas, A.; Rodríguez-Blas, T.; Delgado, R.; Platas-Iglesias, C. Reasons behind the Relative Abundances of Heptacoordinate Complexes along the Late First-Row Transition Metal Series. *Inorg. Chem.* **2014**, *53*, 12859–12869. [[CrossRef](#)]
38. Alvarez, S.; Alemany, P.; Casanova, D.; Cirera, J.; Llunell, M.; Avnir, D. Shape maps and polyhedral interconversion paths in transition metal chemistry. *Coord. Chem. Rev.* **2005**, *249*, 1693–1708. [[CrossRef](#)]
39. Llunell, M.; Casanova, D.; Cirera, J.; Alemany, P.; Alvarez, S. *SHAPE (2.1)*; Universitat de Barcelona: Barcelona, Spain, 2013.
40. Varga, F.; Rajnák, C.; Titiš, J.; Moncol, J.; Boča, R. Slow magnetic relaxation in a Co(ii) octahedral–tetrahedral system formed of a [CoL3]2+ core with L = bis(diphenylphosphanoxido) methane and tetrahedral [CoBr4]2– counter anions. *Dalton Trans.* **2017**, *46*, 4148–4151. [[CrossRef](#)]
41. Rajnák, C.; Titiš, J.; Moncol, J.; Renz, F.; Boča, R. Field-Supported Slow Magnetic Relaxation in Hexacoordinate CoII Complexes with Easy Plane Anisotropy. *Eur. J. Inorg. Chem.* **2017**, *2017*, 1520–1525. [[CrossRef](#)]
42. Titiš, J.; Rajnák, C.; Valigura, D.; Boča, R. Field influence on the slow magnetic relaxation of nickel-based single ion magnets. *Dalton Trans.* **2018**, *47*, 7879–7882. [[CrossRef](#)]
43. Mandal, S.; Mondal, S.; Rajnák, C.; Titiš, J.; Boča, R.; Mohanta, S. Syntheses, crystal structures and magnetic properties of two mixed-valence Co(iii)Co(ii) compounds derived from Schiff base ligands: Field-supported single-ion-magnet behavior with easy-plane anisotropy. *Dalton Trans.* **2017**, *46*, 13135–13144. [[CrossRef](#)]
44. Tupolova, Y.P.; Shcherbakov, I.N.; Popov, L.D.; Lebedev, V.E.; Tkachev, V.V.; Zakharov, K.V.; Vasiliev, A.N.; Korchagin, D.V.; Palii, A.V.; Aldoshin, S.M. Field-induced single-ion magnet behaviour of a hexacoordinated Co(II) complex with easy-axis-type magnetic anisotropy. *Dalton Trans.* **2019**, *48*, 6960–6970. [[CrossRef](#)] [[PubMed](#)]
45. Tupolova, Y.P.; Shcherbakov, I.N.; Korchagin, D.V.; Tkachev, V.V.; Lebedev, V.E.; Popov, L.D.; Zakharov, K.V.; Vasiliev, A.N.; Palii, A.V.; Aldoshin, S.M. Fine-Tuning of Uniaxial Anisotropy and Slow Relaxation of Magnetization in the Hexacoordinate Co(II) Complexes with Acidoligands. *J. Phys. Chem. C* **2020**, *124*, 25957–25966. [[CrossRef](#)]
46. Kosolapoff, G.M.; Roy, C.H. Synthesis of Some Pyrimidylphosphonates. *J. Org. Chem.* **1961**, *26*, 1895–1898. [[CrossRef](#)]
47. Matsnev, M.E.; Rusakov, V.S. SpectrRelax: An application for Mössbauer spectra modeling and fitting. *AIP Conf. Proc.* **2012**, *1489*, 178–185. [[CrossRef](#)]
48. Agilent. *CrysAlis PRO*, version 171.35.19; Agilent Technologies UK Ltd.: Yarnton, UK, 2011.
49. Sheldrick, G.M. *G.M. Sheldrick (8/06/2000). SHELXL v. 6.14, Structure Determination Software Suite*, Bruker AXS: Madison, WI, USA, 2000.

50. Lazarenko, V.A.; Dorovatovskii, P.V.; Zubavichus, Y.V.; Burlov, A.S.; Koshchienko, Y.V.; Vlasenko, V.G.; Khrustalev, V.N. High-Throughput Small-Molecule Crystallography at the 'Belok' Beamline of the Kurchatov Synchrotron Radiation Source: Transition Metal Complexes with Azomethine Ligands as a Case Study. *Crystals* **2017**, *7*, 325. [[CrossRef](#)]
51. Svetogorov, R.D.; Dorovatovskii, P.V.; Lazarenko, V.A. Belok/XSA Diffraction Beamline for Studying Crystalline Samples at Kurchatov Synchrotron Radiation Source. *Cryst. Res. Technol.* **2020**, *55*, 1900184. [[CrossRef](#)]
52. Kabsch, W. XDS. *Acta Crystallogr. Sect. D* **2010**, *66*, 125–132. [[CrossRef](#)]
53. Sheldrick, G. SHELXT-Integrated space-group and crystal-structure determination. *Acta Crystallogr. Sect. A* **2015**, *71*, 3–8. [[CrossRef](#)]
54. Dolomanov, O.V.; Bourhis, L.J.; Gildea, R.J.; Howard, J.A.K.; Puschmann, H. OLEX2: A complete structure solution, refinement and analysis program. *J. Appl. Crystallogr.* **2009**, *42*, 339–341. [[CrossRef](#)]
55. Roos, B.O.; Taylor, P.R.; Siegbahn, P.E.M. A complete active space SCF method (CASSCF) using a density matrix formulated super-CI approach. *Chem. Phys.* **1980**, *48*, 157–173. [[CrossRef](#)]
56. Per, S.; Anders, H.; Björn, R.; Bernard, L. A Comparison of the Super-CI and the Newton-Raphson Scheme in the Complete Active Space SCF Method. *Phys. Scr.* **1980**, *21*, 323.
57. Siegbahn, P.E.M.; Almlöf, J.; Heiberg, A.; Roos, B.O. The complete active space SCF (CASSCF) method in a Newton-Raphson formulation with application to the HNO molecule. *J. Chem. Phys.* **1981**, *74*, 2384–2396. [[CrossRef](#)]
58. Angeli, C.; Cimiraglia, R.; Evangelisti, S.; Leininger, T.; Malrieu, J.P. Introduction of n-electron valence states for multireference perturbation theory. *J. Chem. Phys.* **2001**, *114*, 10252–10264. [[CrossRef](#)]
59. Angeli, C.; Cimiraglia, R.; Malrieu, J.-P. N-electron valence state perturbation theory: A fast implementation of the strongly contracted variant. *Chem. Phys. Lett.* **2001**, *350*, 297–305. [[CrossRef](#)]
60. Angeli, C.; Cimiraglia, R. Multireference perturbation configuration interaction V. Third-order energy contributions in the Møller-Plesset and Epstein-Nesbet partitions. *Theor. Chem. Acc.* **2002**, *107*, 313–317. [[CrossRef](#)]
61. Angeli, C.; Cimiraglia, R.; Malrieu, J.-P. n-electron valence state perturbation theory: A spinless formulation and an efficient implementation of the strongly contracted and of the partially contracted variants. *J. Chem. Phys.* **2002**, *117*, 9138–9153. [[CrossRef](#)]
62. Hess, B.A. Relativistic electronic-structure calculations employing a two-component no-pair formalism with external-field projection operators. *Phys. Rev. A* **1986**, *33*, 3742–3748. [[CrossRef](#)]
63. Pantazis, D.A.; Chen, X.Y.; Landis, C.R.; Neese, F. All-electron scalar relativistic basis sets for third-row transition metal atoms. *J. Chem. Theory Comput.* **2008**, *4*, 908. [[CrossRef](#)]
64. Schafer, A.; Huber, C.; Ahlrichs, R. Fully optimized contracted Gaussian basis sets of triple zeta valence quality for atoms Li to Kr. *J. Chem. Phys.* **1994**, *100*, 5829–5835. [[CrossRef](#)]
65. Schafer, A.; Horn, H.; Ahlrichs, R. Fully optimized contracted Gaussian basis sets for atoms Li to Kr. *J. Chem. Phys.* **1992**, *97*, 2571–2577. [[CrossRef](#)]
66. Weigend, F.; Ahlrichs, R. Balanced basis sets of split valence, triple zeta valence and quadruple zeta valence quality for H to Rn: Design and assessment of accuracy. *Phys. Chem. Chem. Phys.* **2005**, *7*, 3297–3305. [[CrossRef](#)] [[PubMed](#)]
67. Neese, F. An improvement of the resolution of the identity approximation for the formation of the Coulomb matrix. *J. Comput. Chem.* **2003**, *24*, 1740–1747. [[CrossRef](#)] [[PubMed](#)]
68. Ganyushin, D.; Neese, F. First-principles calculations of zero-field splitting parameters. *J. Chem. Phys.* **2006**, *125*, 024103. [[CrossRef](#)] [[PubMed](#)]